16th ICAAR
LISBOA 2020-2022

16th International Conference on
Alkali-Aggregate Reaction in Concrete
Lisboa | LNEC | Portugal | 31 May - 2 June 2022

http://icaar2020-2022.lnec.pt

Monitoring of ASR affected samples using different NDT-techniques

S.N. Iliopoulos [1], A. Lamberti [2], K. Schildermans [3], S. Ben Hadj Hassine [4]

(1) ENGIE Laborelec, Linkebeek, Belgium, Sokratis.Iliopoulos@engie.com

(2) ENGIE Laborelec, Linkebeek, Belgium, Alfredo.Lamberti@engie.com

(3) ENGIE Laborelec, Linkebeek, Belgium, Kim.Schildermans@engie.com

(4) NIRAS-ONDRAF, Brussels, Belgium, R.Gaggiano@nirond.be

Abstract

The Alkali-Silica Reaction (ASR) gel observed in a few cemented radioactive effluent drums revealed the need for the early detection and monitoring of the phenomenon. Towards this direction three nondestructive testing (NDT) techniques were investigated, namely the Acoustic Emission (AE), the Infrared Thermography (IRT) and the microwave analysis (µWA). The techniques were applied in lab to nine concrete materials combining three different types of aggregates and three different batching solutions. The 6-month results showed that AE was a powerful technique capable of continuously monitoring and identifying differences between ASR affected and non-affected samples for long periods. ASR affected samples produced more acoustic emissions compared to the sound ones, they showed a nonlinear behavior and eventually higher average frequency (AF) values. The analysis of the IRT data confirmed the capability of the technique to detect ASR products, especially when the IR camera had direct access to the side of the concrete samples showing exposed aggregates. From the evaluation of µWA data, significant differences between the reactive and non-reactive samples were showcased. The differences were visible both in time and as a function of frequency and were associated to the amount of free and bound water which varies relatively to the extent of ASR.

Keywords: *acoustic emission (AE); alkali-silica reaction (ASR); microwave-analysis, non-destructive testing (NDT); thermograph*

1. INTRODUCTION

During a routine inspection in 2013, a gel-like substance was observed in a few cemented radioactive effluents drums. Analysis showed that this gel-like substance was caused by the alkali-silica reaction (ASR). In order to be able to determine which drums are affected, an 18-month study was launched in January 2019 to investigate non-destructive testing (NDT) techniques that are able to detect and monitor ASR. The study concerned three techniques: Acoustic Emission (AE), Infrared Thermography (IRT) and microwave analysis (µWA).

Nine materials were tested using all three techniques. The concrete recipes combined three types of aggregates (limestone, non-reactive siliceous aggregates and reactive siliceous aggregates) with three batching solutions (tap water, a solution mimicking the waste composition and a ($NaOH+NaNO_3$) solution with the same sodium content as the latter).

The AE results were promising. A distinction in activity was seen between the active and the non-active samples. The number of cumulated hits received by the AE sensors in the first case was considerably higher compared to the second case. Apart from the number of emissions, differences between the active and non-active samples were also observed on the daily rate of AE hits as well as on other sensitive AE parameters such as the average frequency.

The analysis of the IRT data pinpointed the capability of the technique to detect ASR products. The probability of detection was, however, higher when looking at the inner-surface where the aggregates were exposed and directly accessible by the IR camera and lower when the outer-surface was inspected. The images clearly showed that the aggregates are affected and degraded over time.

From the evaluation of µWA data, significant differences between the reactive and non-reactive samples were showcased. The differences were visible both in time and as a function of frequency and were associated to the amount of free and bound water which varies relatively to the extent of ASR.

2. ALKALI-SILICA REACTION (ASR)

The ASR is a chemical reaction between (1) hydroxyl ions (OH-) in the alkaline cement pore solution of the concrete and (2) reactive forms of silica in the aggregate. The reaction yields into a hygroscopic gel, which expands as it absorbs water. The characteristics of the resulting gel largely depend on the composition of the pore water solution, the temperature and the concentration of the reactants.

The ASR takes place in four stages [1], [2], [3]:

1. Hydrolysis of the reactive silica by the OH- leading to the formation of an alkali-silica gel
2. Increase of gel volume, due to water absorption
3. Micro-cracking [1] near the reaction site, due to swelling pressures resulting from the volume increase
4. Propagation and coalescence of micro-cracks, formation of macro-cracks.

Although ASR is a well-known reaction in concrete science, some doubt still exists concerning its initiation and propagation mechanisms. One theory suggests that the aggregate is dissolved from the inside and that as the aggregate dissolves it absorbs water which leads to micro-cracking. This micro-cracking then leads to macro-cracking as gel-expansion continues (see Figure 2.1). A second theory suggests that a layer of dissolved silica is formed at the interface zone (note: the interface between the aggregate and the cement). This layer then absorbs water and expands causing cracking in the cement (see Figure 2.2).
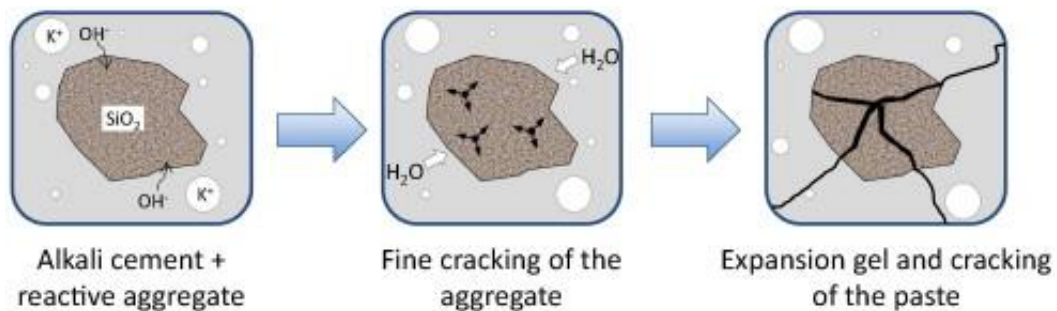

Figure 2.1: Possible alkali-silica reaction mechanism consisting of 3 steps and originated inside the aggregate [2]
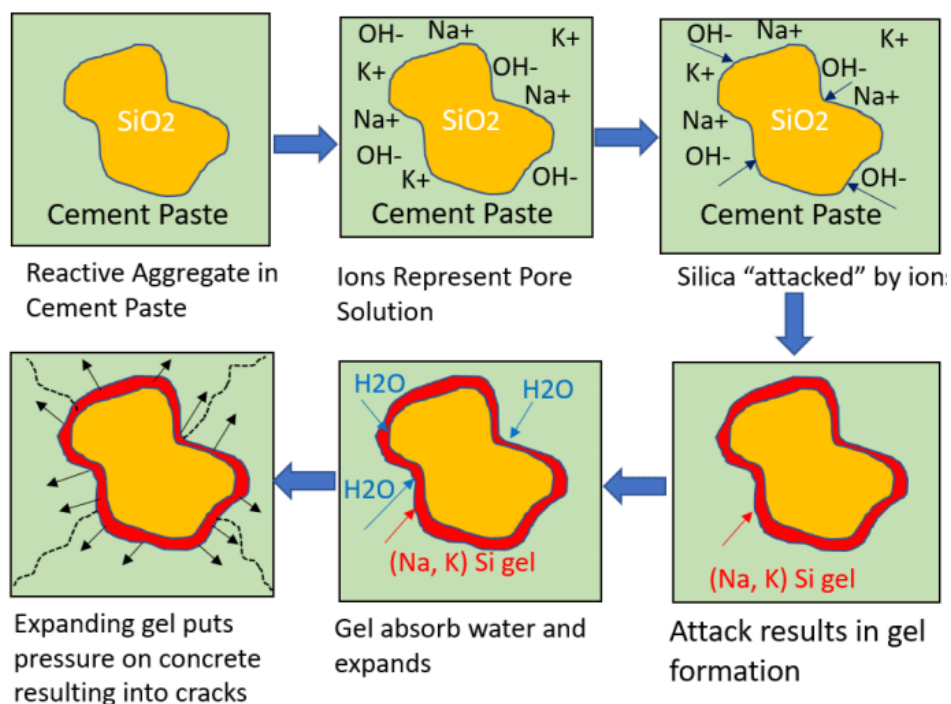

Figure 2.2: Possible mechanism for step 1 through 6 of the alkali silica reaction [3]

3. MATERIALS

In this study, nine different concrete recipes were investigated. The concrete recipes combined three types of aggregates (limestone non-reactive aggregates - A0, reactive siliceous aggregates – A1 and non-reactive siliceous aggregates – A2) with three batching solutions (tap water – C0, a (NaOH+NaNO$_3$) solution – C1 and a solution mimicking the waste composition – C2) [see Table 3.1]. C1 and C2 have the same sodium concentration. Additionally, to better represent the cemented radioactive waste packages, the C2 batching solution was heated up to 60°C and a thermal cycle was applied to all samples batched with the C2 solution during the two weeks following batching. This thermal cycle was based on temperature measurements within three different drums that were produced during cementation campaigns of the real radioactive waste. Each recipe was used for the casting of two cubes (in total 18 cubes) each of which was cut in two samples (in total 36 samples). The non-destructive testing of the 18-month experimental campaign included the monitoring of the 27 concrete samples having the following dimensions: 150 mm x 150 mm x 75 mm.

Table 3.1: The nine recipes (A0C0 to A2C2) in this study combine three types of aggregates (A0, A1, A2) and three types of pore water solution (C0, C1, C2).

		Pore water solution		
		C0	**C1**	**C2**
Aggregate	**A0**	A0C0	A0C1	A0C2
	A1	A1C0	A1C1	A1C2
	A2	A2C0	A2C1	A2C2

4. SELECTED NDT TECHNIQUES

4.1 Acoustic Emission (AE)

AE is a real time monitoring technique capable of detecting wave signals. The signals, which are typically produced by cracking or other irreversible changes (e.g. formation of ASR products) [4] propagate in all directions in the form of elastic waves. When the waves reach the surface of the materials, suitable transducers that are attached to this surface record the transient response. The transducers are usually piezoelectric and their main function is to transform the mechanical pulse into an electric waveform, which is then amplified, digitized and stored for real time analysis and post-treatment.

AE is very powerful and was used in this experimental campaign since it supplies information in different aspects; the most important one is that the accumulated activity is related to the "density" of cracks [4]. AE enables to monitor the fracture process from the initiation of the micro-cracks to the development of the macro-cracks. Apart from the number of emissions, the transient elastic waves that are emitted at the tip of the crack contain important information on the motion of the crack sides and the severity of active cracking [5] - [10].

The wave signals constitute the raw AE data. Post-processing of the raw data includes the enumeration and decomposition of the AE waveforms into its parameters, as well as the representation of the latter in time or in combination with each other. The most important/sensitive parameters are illustrated in Figure 4.1.
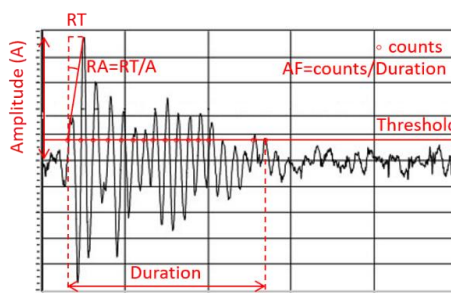

Figure 4.1: Typical AE waveform and its main parameters

4.2 Infrared Thermography (IRT)

In Infrared Thermography (IRT), an infrared camera is used to inspect a test object. The output of the IR camera is an image called thermogram. A thermogram can be considered as a function T(x,y), with (x,y) scalar positive values indicating the spatial coordinates and an amplitude T corresponding to the temperature. The function T(x,y) is continuous in space and amplitude and can be digitally converted by sampling in both space and amplitude. Space sampling is defined by the resolution of the IR camera, i.e. the number of rows and columns constituting the IR detector (640 x 480 in this study). The amplitude sampling, generally referred to as quantization (or dynamic range), is the number of bits used to represent a discrete value of measured IR radiation (16bit in this study).

IRT is associated with many parameters. In this study, the sample temperature T_s is considered. The temperature T_s measured by the IR camera is a parameter that relies on different other parameters, like the total radiation received by the camera (W_{tot}), the emissivity of the sample (ε_s), the reflected temperature (T_r), the transmittance of the atmosphere (τ_{atm}) and the temperature of the atmosphere (T_{atm}) [11]. The τ_{atm} is very close to 1 rendering the atmospheric contribution negligible. The emissivity contribution is, however, significant. The ε_s value used for this work is 0.95, for all the samples under investigation.

Post-processing of the raw data in this study concerns the computation of the Principal Components (PCs) [11]. The latter reduces the dimension of the data set keeping at the same time the features that contribute the most to the variance of the data set. Therefore a sequence of several dozens of thermograms can be compressed in few PCs that may show the essence of the sample. PC analysis decomposes data into a set of orthogonal statistical modes obtained through singular value decomposition (SVD). For each PC$_r$, it is possible to retrieve its variance contribution rate α_r. When the variance cumulative contribution $\varphi(q) = \sum_{i=1}^{q} a_i$ of the first q PCs is more than a pre-set threshold (99% in this study), the original information contained in the sequence of thermograms can be sufficiently reflected. In this paper, the PCA weighted sum = $\sum_{i=1}^{q} PC_i . a_i$ is used. The presence of ASR on the test sample induces local colour variations in the PCA weighted sum images due to variance induced by the ASR evolution in the thermogram series.

4.3 Microwave Analysis (µWA)

At microwave frequencies, the macroscopic electrical behavior of concrete is described by the dielectric constant. The dielectric constant is a complex parameter. The real part of this complex quantity, referred to as relative permittivity, indicates the ability of the material to be polarized or store microwave energy. The imaginary part, referred to as relative loss factor, indicates the ability of the material to absorb microwave energy. The latter is an intrinsic parameter, yielding information about material properties and changes and is independent of how it is measured. Evaluation of material changes with time (e.g. due to development of ASR) involve measuring the complex (magnitude and phase) reflection and transmission coefficients of a microwave signal interacting with the dielectric material.

In this paper, among all the parameters, the magnitude of the complex transmission coefficient S$_{12}$ is presented. S$_{12}$ gives an indication of the signal transmitted through the sample and its attenuation caused by the sample. The attenuation depends on the samples chemical composition (e.g. free vs. bound water and the presence of ASR) and physical properties. Higher S$_{12}$ (less negative) represents less signal attenuation through the sample (less free water content within the sample pores).For the link between S$_{12}$ and the dielectric constant the reader is referred to [12].

5. EXPERIMENTAL SETUP

In the framework of this study, ENGIE Laborelec designed and built a setup that allowed the storage of 27 affected and non-affected by ASR samples (Figure 5.1-left). The setup functioned as a climate chamber offering controlled humidity and temperature conditions (100 % and 38 ˚C respectively) as well as the room where AE could be continuously applied.

The length of the custom made climate chamber was 1200 mm while the height and width were 1650 mm and 790 mm respectively (Figure 5.1-right). Figure 5.1-left provides a view of the samples topology in the climate chamber. As shown there, the samples are arranged in 3 rows (L1 (top), L2 (middle), L3 (bottom)) and 9 columns. The following should be mentioned:

■ L1 is continuously equipped with AE sensors and the AE behavior of all 9 recipes is continuously monitored for 18 months,

■ AE Sensors 8, 10 and 16 change position each week from L2 to L3 for statistical and uniformity-evaluation reasons,

■ IRT and µWA are discretely and alternately performed each week between the samples of L2 and L3 for statistical and uniformity-evaluation reasons,

■ Each of the 9 columns corresponds to one of the 9 different recipes used in this study (see Table 3.1),

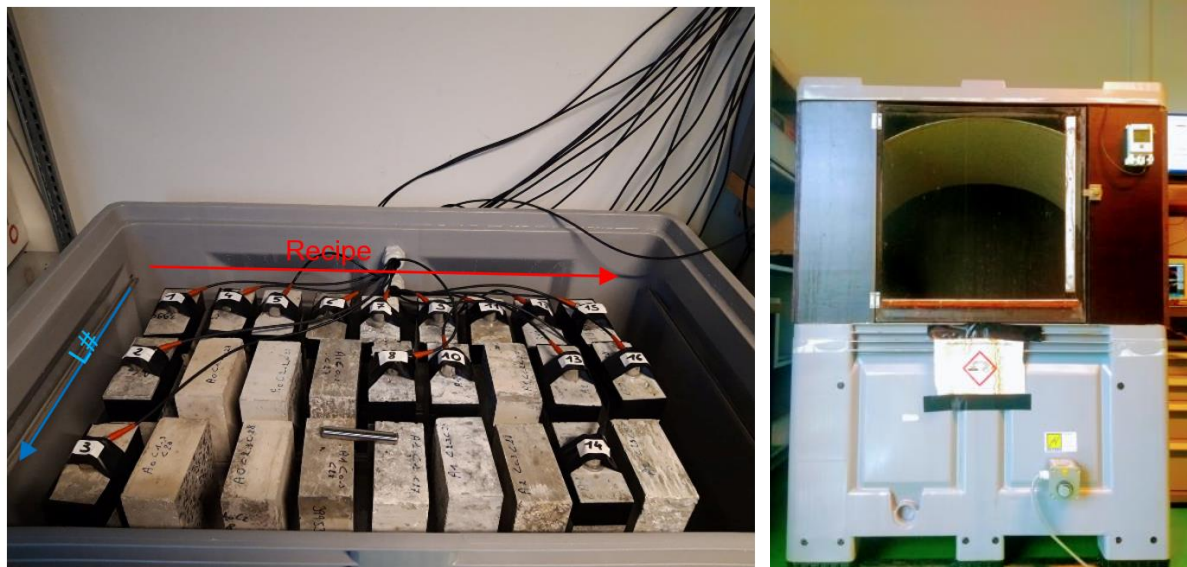■ Each row corresponds to one of the 3 samples of the same recipe.

Figure 5.1 Left: Topology of the samples in the climate chamber, Right: Exterior of the chamber

Concerning AE the R15I-AST sensors were used. The sensors had a resonance frequency equal to 150 kHZ and were equipped with an integral preamplifier. For the data acquisition the Micro-II Express system (Express-8 Digital AE system) was used. The aforementioned data acquisition system enabled powerful AE testing capabilities and holded 16 channels.

For the IRT measurements the FLIR A655sc camera was used. The aforementioned used an uncooled microbolometer detector, had 16-bit dynamic range and 7.5-14 micrometers spectral range (LWIR). The measurements were performed once a week after taking out of the climate chamber one by one the samples of L2 or L3. The infrared inspection of each sample lasted 30 min.

For the µWA data acquisition the E5061B LF-RF Network analyzer was used. The E5061B LF-RF Network analyzer offers a versatile network analysis in the broad frequency range from 5 Hz to 3 GHz as well as it comes with two S-parameter test ports and an impedance analysis function. Similarly to IRT, the measurements were performed once a week after taking out of the climate chamber one by one the samples of L2 or L3.

6. RESULTS AND DISCUSSION

6.1 Acoustic Emission (AE)

Each signal received by the AE sensor at the concrete surface corresponds to an AE hit. Summing up the hits and presenting them as a function of time results in the so called "*Cumulative AE hits curves*". Figure 6.1 illustrates these curves in triplets for all 9 samples. The data represent the first 6-months of the AE acquisition (week 0 to week 24). The total number of AE hits is related to the amount of cracks. The higher the cumulated hits the higher the activity and thus the higher the severity of the process in place.

Two samples can have the same total number of hits but different rates. The changes in the AE behavior are, thus, better visualized through the *#Hits/Day* parameter (Figure 6.2). To calculate this parameter, the AE hits of each day are counted and presented in time. The result indicates the speed of reaction.
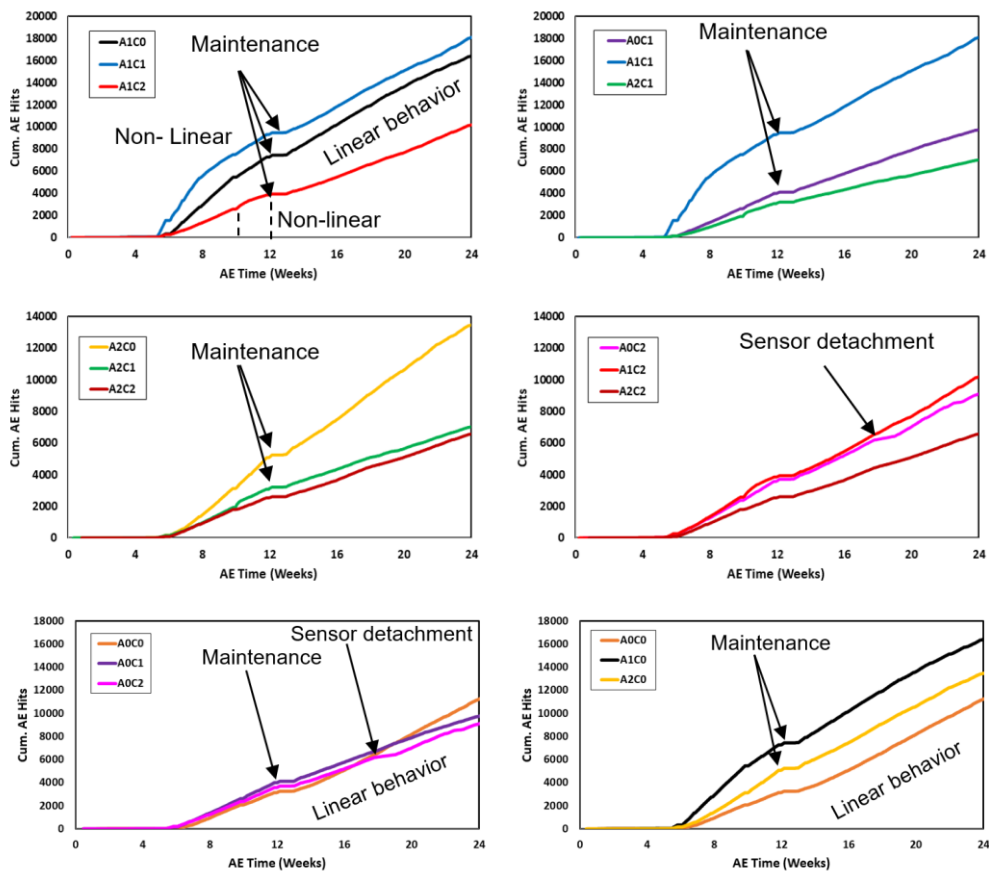
Figure 6.1: Influence of the solution chemistry (fixed aggregate type, on the left column) and the aggregate type (fixed solution chemistry, on the right column) on the cumulative AE Hits curves.

The higher the number of AE hits/day the higher the slope of the cumulative AE hits curves and the faster the reactions that take place.
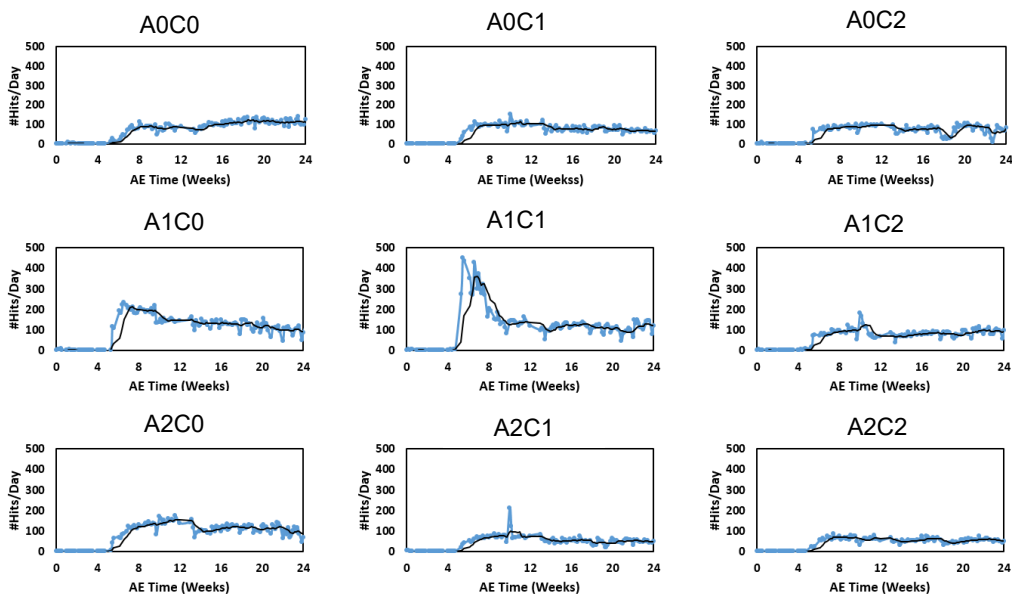

Figure 6.2: Daily rate of AE Hits for all the recipes during the first 6 months of acquisition (week 0 to week 24). The black line is a moving average trend line over 7 points.

Figure 6.3 shows the evolution of the Average Frequency (AF) parameter as a function of time from week 0 (beginning of AE acquisition) to week 24 (6 months). The data correspond to L1 samples (see Figure 5.1-left). For better visualization of the extreme amount of scattered data, a moving average is used (see red line). In Figure 6.3 indicative graphs are presented. The graphs are the following: A0C1 as reference, A1C1 as the most reactive (both from the composition and the AE hits point of view), A1C2 and A2C1 due to the non-linear behavior presented in Figure 6.1 and Figure 6.2.

The most important findings obtained from Figure 6.1, Figure 6.2 and Figure 6.3 are summarized in Table 6.1.

Table 6.1 Summary of results and findings obtained from Figure 6.1 and Figure 6.2.

| Sample	Observations
A1C0 – A1C1 – A1C2	A1C1 has the highest emissions and the highest daily rate of all three samples (in general of all 9) rendering it the most reactive recipe from the cumulative AE hits and the *#Hits/Day* point of view. The nonlinear behavior of A1C1 is present from week 6 to week 10. The deviation from linearity is related to ASR in this study. Moreover, A1C1 has constantly higher AF values (approximately 60 kHz). The initial AF value is approximately 70 kHz while the trend is decreasing implying severe ASR evolving with time. A1C2 has lower hits than A1C1 and A1C0 possibly due to the fact that the sample was earlier subjected to a thermal cycle (Kaiser effect) [13]. The slope of A1C2 changes on week 10 for 1.5 days. This slope change is attributed to ASR. The latter was confirmed visually and with IRT. Concerning the AF behavior, A1C2 has generally constant behavior with slightly higher values than A0C1. AF is rapidly increasing on week 10 implying ASR activity. The maximum rate of AE hits for A1C0 and A1C1 is higher than the rate of the corresponding reference samples (A0C0 and A0C1 respectively). All samples show a constant very low evolution rate at the beginning of the acquisition followed by a rapid increase of the hits rate on week 5.
A0C1 – A1C1 – A2C1	A0C1 shows a constant AF vs. time behavior (AF approximately 50 kHz) implying no ASR. A2C1 produces lower emissions than A0C1. A2C1 changes slope on week 10 for 1.5 days (similarly to A1C2). This change of slope is an indication of ASR. The change of slope is seen on the *#Hits/Day* curve as well as on the AF vs Time curve.
A2C0 – A2C1 – A2C2	A2C2 has the lowest hits due to the fact that it was thermally loaded before the start of the experimental campaign (Kaiser effect) [13]. A2C1 has more hits than A2C2 but still below the reference (by composition) A2C0. The latter (A2C0) shows similar AE behavior and equivalent values to the reference (in terms of composition) recipes.
A0C2 – A1C2 – A2C2	A1C2 has the most hits of the three samples due to the reactive combination of A1 aggregates and the alkalis contained in the C2 chemistry of the solution. A0C2 has lower hits compared to A1C2 due to the non-reactive aggregates. A2C2 has the lowest activity because of being thermally pre-loaded (despite the potentially reactive nature of the A2 aggregate).
A0C0 – A0C1 – A0C2	Same number of emissions implying similar behavior. Similar trends for all recipes (linear).
A0C0 – A1C0 – A2C0	Similar trends for all recipes (linear). The linear trend implies non-ASR behavior. A1C0 shows higher activity than A2C0 and A2C0 shows higher activity than A0C0.
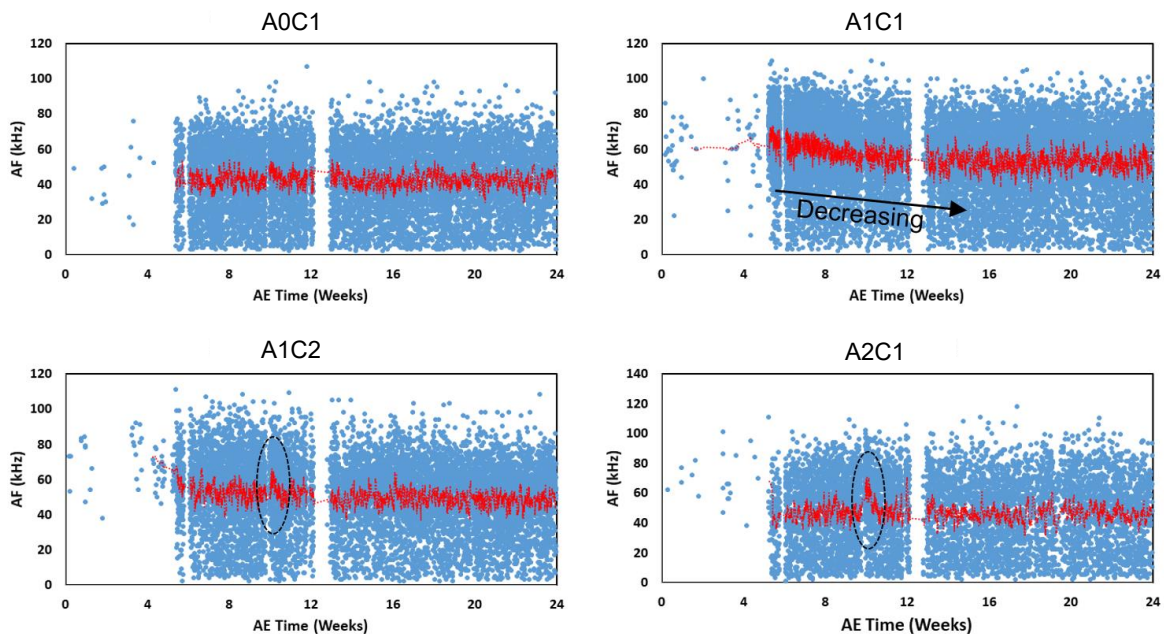
Figure 6.3: Time evolution of the AF parameter for 4 indicative cases.

6.2 Infrared Thermography (IRT)

Table 6.2 presents a summary of the results and findings using IRT. The findings correspond to all 9 recipes. Figure 6.4 presents 4 indicative cases (A0C0, A1C1, A1C2 and A2C2). A0C0 was selected for its reference behavior while the other three due to the clear signs of ASR.

Table 6.2: Summary of Results and Findings of IRT inspection

| Sample	Observations
A0C0 – A0C1 – A0C2 A1C0 – A2C0 – A2C1	The PCA weighted sum is consistent during the weeks (no color spots appearing in the weighted PCA images from one week to another), meaning that no evident effects of ASR products are detectable (see indicatively the inside view of A0C0 sample of L2 on Figure 6.4).
A1C1 – A1C2 – A2C2	Clear signs of possible ASR products are visible. The A1C1 and A1C2 samples appear to be the most affected ones. ASR effects are clear on the inner-surface of both samples (Figure 6.4 top right, Figure 6.4 bottom left) but cannot be detected on the outer-surface (Figure 6.4 bottom left). The ASR products appear on the samples placed on L2 and on those placed on L3. Herein, indicatively, for A1C1 the sample of L2 is shown and for A1C2 and A2C2 the samples of L3. The A2C2 sample shows signs of possible ASR. Indications are visible on the inner-surface on L2 as well as on that on L3 (indicatively shown in Figure 6.4). The outer-surface of the A2C2 sample on L3 (Figure 6.4-bottom right) shows large spots which are believed to be associated with ASR. Conversely, no ASR signs seem to appear on the outer-surface of the A2C2 sample on line 2.
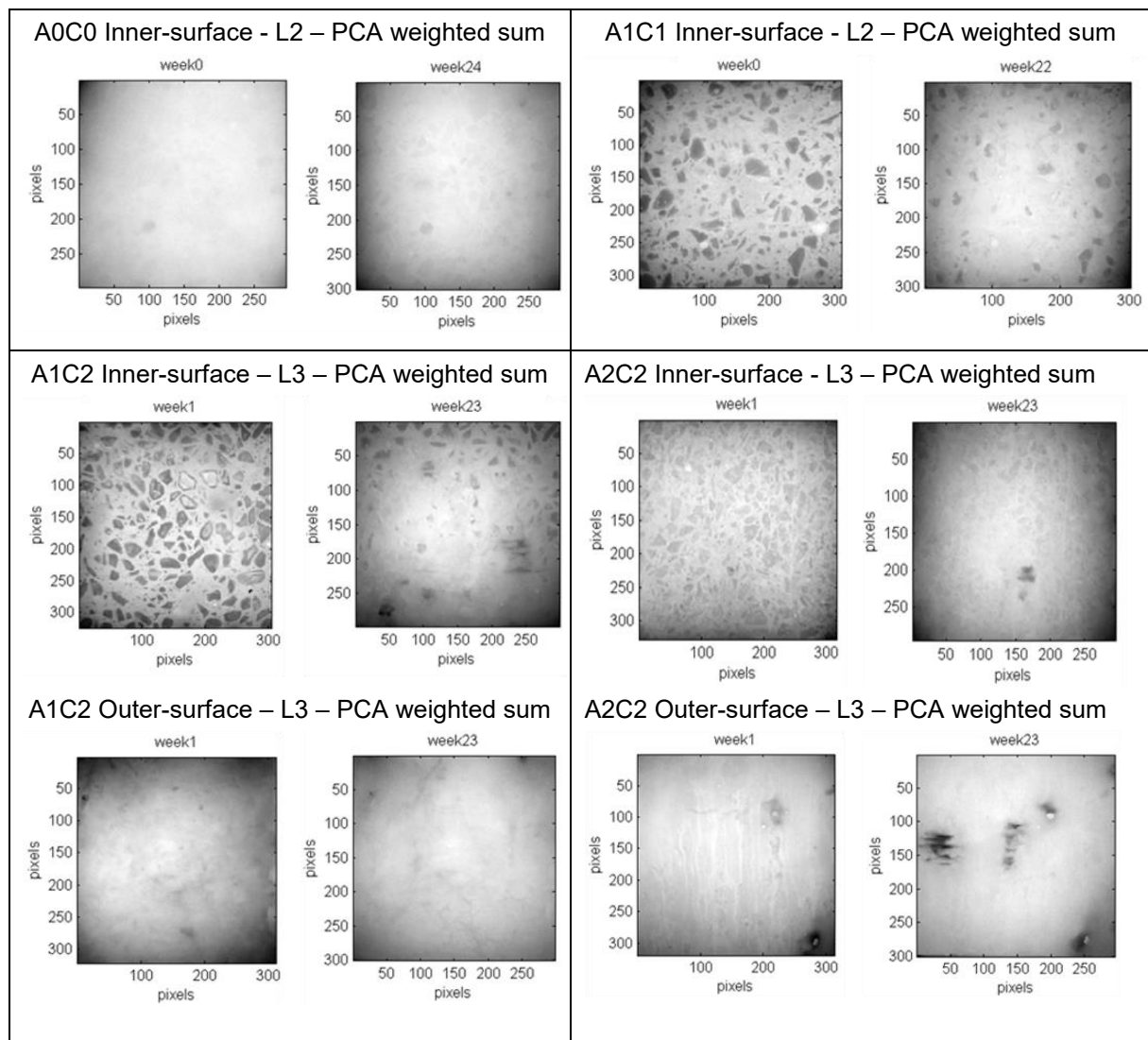
Figure 6.4: Evolution of the PCA weighted sum for 4 indicative cases.

6.3 Microwave Analysis (µWA)

Figure 6.5 shows the temporal evolution of the S_{12} transmission coefficient (expressed in dB) as a function of frequency (in MHz) for the reference, non-reactive sample A0C0 and the most reactive (based on composition) sample, A1C1. The frequency ranges from 100 kHz to 1 MHz and is presented in logarithmic scale. The samples correspond to L2 in the climate chamber.

Considering the results of Figure 6.5, important differences between the reactive and non-reactive samples are evident (same scale has been used for direct comparisons). The measured S_{12} coefficient is clearly different for the two samples both in time and as a function of frequency. For all the frequencies, the S_{12} coefficient of the non-reactive A0C0 sample is lower (more negative) than that of the reactive sample by approximately 3-6 dB (where 3 dB represents a signal power decrease by 50 %). This difference is significant and is due to the fact that the free moisture content in the non-reactive sample is higher than that of the reactive.

In order to better visualize the differences between the reactive and non-reactive samples, the results of Figure 6.5 are presented as a function of time for the fixed frequency of 100 kHz. The time axis is expressed in weeks, starting from week 6 (beginning of the microwave acquisition) and ending on week 24 (6-months). The measurements on the same sample are repeated every two weeks. In-between, the line of measurement changes from L2 to L3.

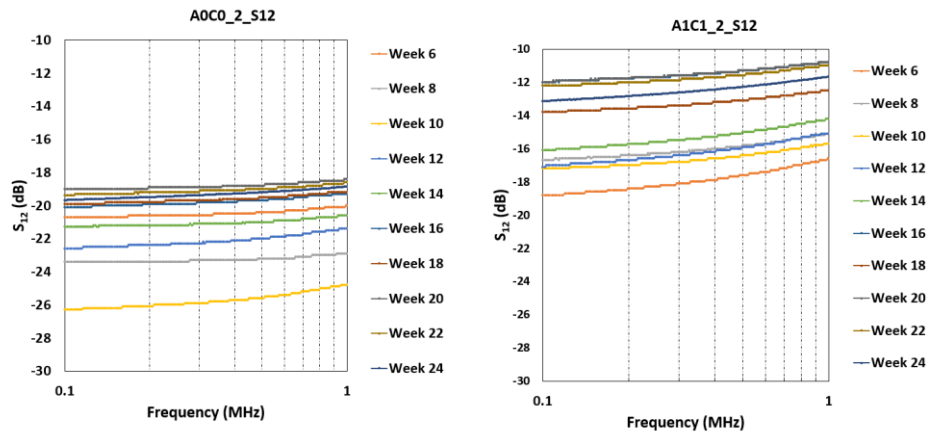Table 6.3 summarizes the most important observations.

Figure 6.5: Temporal evolution of the S_{12} transmission coefficient as a function of frequency for a) the non-reactive reference sample A0C0 and b) the most reactive sample A1C1 of line 2.
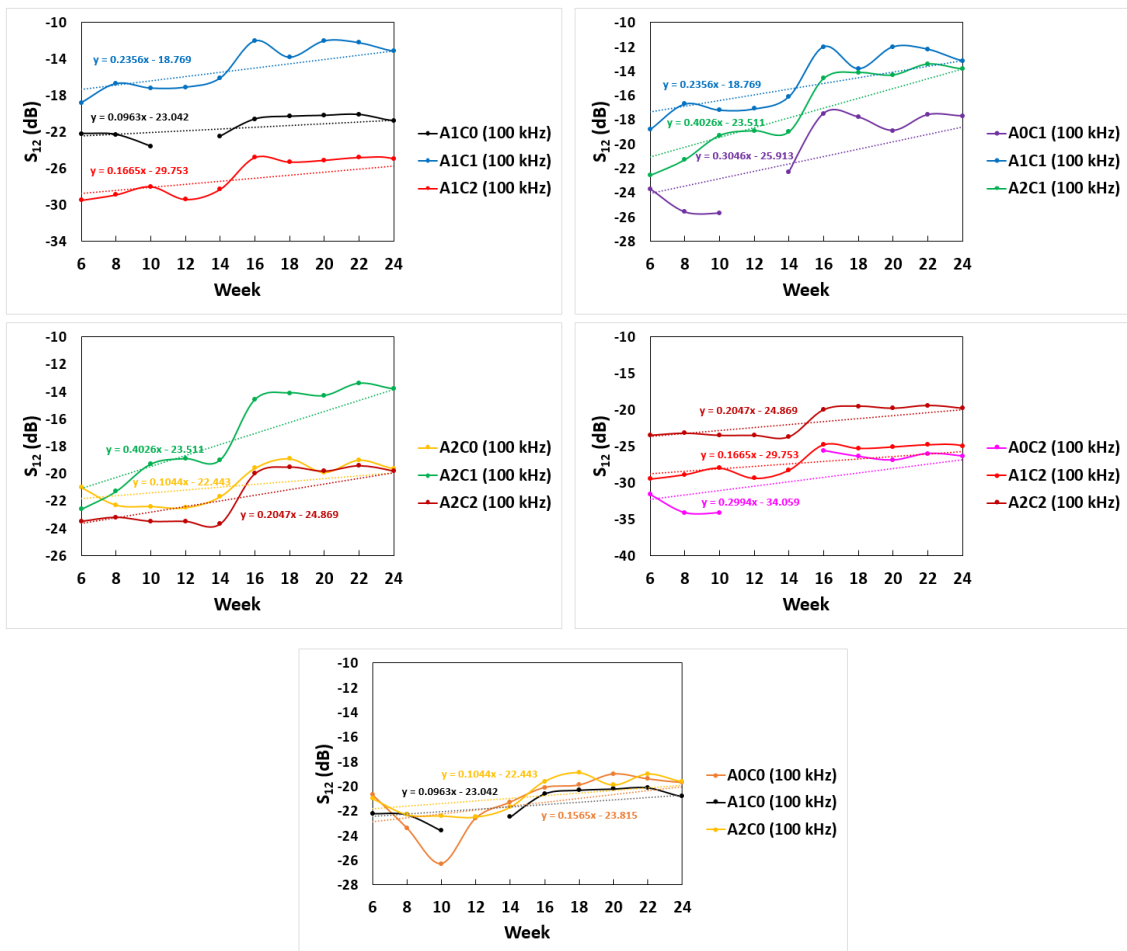

Figure 6.6: Influence of the aggregate type and the pore water solution on the temporal evolution of S_{12} for the samples of line 2

Table 6.3: µWA observations of the behavior of reactive and no-reactive samples

Sample	Observations
A0C0 – A1C0 – A2C0	All three samples contain tap water (C0 solution). Thus, no ASR is expected to occur. The latter can be elaborated by the very slow time evolution of the S_{12} parameter (almost constant values). It is also interesting to note that for all three sample the S_{12} values are close to each other implying similar macroscopic behavior.
A1C0 – A1C1 – A1C2	The A1C0 sample shows an almost constant behavior in time (slope approximately 10 %) verifying the non-reactive nature of the sample. On the other hand, the A1C1 and A1C2 samples show continuously increasing trends implying water uptake and bounding. Among the reactive samples A1C1 and A1C2 the first seems more affected by ASR if we consider the higher slope (0.24 compared to 0.17) and the higher S_{12} values (less negative - less attenuation).
A0C1 – A1C1 – A2C1	All three samples show significant increasing trends. In the case of A2C1 the slope is up to 4 times higher than that of the reference A0C0 sample indicating a very rapid water uptake and bounding. The - attributed to ASR- difference between A1C1 and A0C1 is evident when one observes the higher S_{12} values in the first case.
A2C0 – A2C1 – A2C2	The temporal evolution of A2C0 and A2C2 is similar (values very close to each other for the samples of line 2 and same slopes for the samples of line 3). It is reminded that A2C0 is considered non-reactive due to the tap water used as batch solution. From the µWA point of view, A2C1 is the most reactive sample as indicated by the very high inclination angles and the low S_{12} values.
A0C2 – A1C2 – A2C2	All three samples show similar trends with slopes varying from 0.17 to 0.30. Looking at the S_{12} values and the associated ranking of the samples, A0C2 is the least reactive (as expected due the A0 type of aggregate), A2C2 more reactive and A1C2 in between the two.

7. CONCLUSIONS

The current paper presents the results of the first 6 months of the 18-month experimental campaign. The aim of the experimental campaign was to investigate non-destructive testing (NDT) techniques that are able to detect and monitor ASR. Three NDT techniques were used in this study: Acoustic Emission (AE), Infrared Thermography (IRT) and microwave analysis (µWA). AE contains many powerful parameters that can distinguish the behavior of ASR affected and non-affected samples, while as shown in this study, the technique is very sensitive to the presence of reactive siliceous aggregates. IRT is useful for the visualization of the phenomenon in case the aggregates are visible. µWA is capable of identifying sample differences related to the amount of free and bound water. Table 7.1 summarizes the ASR alarm level for each of the 3 different NDT techniques and each of the 9 different samples. The green color illustrates that ASR is not present. The red illustrates signs of ASR observed with the corresponding technique. Orange corresponds to indications that are not clear. The final aim of the research study is to quantify ASR destructively and correlate it with the NDT observations.

Table 7.1: Summarizing table providing the probability of occurrence of ASR. The conclusions are based on the observations obtained from three different NDT techniques: AE, IRT and µWA. Green indicates no ASR signs with the corresponding technique, orange signifies possible ASR signs, while red corresponds to ASR indications.

Sample	AE	IRT	µWA
A0C0	green	green	green
A0C1	green	green	orange
A0C2	green	green	orange
A1C0	green	green	green
A1C1	red	red	red
A1C2	orange	red	orange
A2C0	green	green	green
A2C1	orange	green	red
A2C2	green	red	orange

8. REFERENCES

[1] R. N. Swamy and M. M. Al-Asali, "Engineering properties of concrete affected by alkali-silica reaction," ACI Mater. J., vol. 85, no. 5, pp. 367–374, 1988.

[2] M. Abdelrahman, M. K. ElBatanouny, P. Ziehl, J. Fasl, C. J. Larosche, and J. Fraczek, "Classification of alkali–silica reaction damage using acoustic emission: A proof-of-concept study," Constr. Build. Mater., vol. 95, pp. 406–413, 2015.

[3] Lima, Mehdi. (2018). CFRP Strengthening of ASR Affected Concrete Piers of Railway Bridges.

[4] C. U. Grosse and M. Ohtsu, Acoustic emission testing. Springer Science & Business Media, 2008.

[5] N. Alver, H. M. Tanarslan, O. Y. Sulun, E. Ercan, M. Karcl, E. Selman, and K. Ohno, Effect of CFRP-spacing on fracture mechanism of CFRP-strengthened reinforced concrete beam identified by AESiGMA, Construction and Building Materials, vol. 67, pp. 146-156, 2014.

[6] A. Behnia, H. K. Chai, and T. Shiotani, Advanced structural health monitoring of concrete structures with the aid of acoustic emission, Construction and Building Materials, vol. 65, pp. 282-302, 2014.

[7] S. Muralidhara, B. R. Prasad, H. Eskandari, and B. L. Karihaloo, Fracture process zone size and true fracture energy of concrete using acoustic emission, Construction and Building Materials, vol. 24, no. 4, pp. 479-486, 2010.

[8] T. Shiotani, J. Bisschop, and J. Van Mier, Temporal and spatial development of drying shrinkage cracking in cement-based materials, Engineering Fracture Mechanics, vol. 70, no. 12, pp. 1509-1525, 2003.

[9] Y. Kawasaki, T. Wakuda, T. Kobarai, and M. Ohtsu, Corrosion mechanisms in reinforced concrete by acoustic emission, Construction and Building Materials, vol. 48, pp. 1240-1247, 2013.

[10] A. Zaki, H. K. Chai, D. G. Aggelis, and N. Alver, Non-destructive evaluation for corrosion monitoring in concrete: A review and capability of acoustic emission technique, Sensors, vol. 15, no. 8, pp. 19069-19101, 2015.

[11] Infrared Thermography for Temperature Measurement and Non-Destructive Testing, Sensors 2014, 14, 12305-12348; doi:10.3390/s140712305

[12] Kim, S., & Baker-Jarvis, J. (2014). An approximate approach to determining the permittivity and permeability near lambda/2 resonances in transmission/reflection measurements. Progress In Electromagnetics Research, 58, 95-109.

[13] Dejian, Wu Shengxing Zhang Shunxiang Shen. "An experimental study on Kaiser effect of acoustic emission in concrete under uniaxial tension loading [J]." China Civil Engineering Journal 4 (2008).